Nano Research
2020, 13(12): 3377–3386
ISSN 1998-0124 CN 11-5974/O4
https://doi.org/10.1007/s12274-020-3025-0

Research Article

Core–satellite metal–organic framework@upconversion nanoparticle superstructures via electrostatic self-assembly for efficient photodynamic theranostics

Zhike Li[1], Xi Qiao[1], Guihua He[1], Xin Sun[1], Danhua Feng[1], Liefeng Hu[1], Hua Xu[2], Hai-Bing Xu[3], Shengqian Ma[4] (✉), and Jian Tian[1] (✉)

[1] *Key Laboratory of Combinatorial Biosynthesis and Drug Discovery, Hubei Province Engineering and Technology Research Center for Fluorinated Pharmaceuticals, School of Pharmaceutical Sciences, Wuhan University, Wuhan 430071, China*
[2] *State Key Laboratory of Bioelectronics, School of Biological Science and Medical Engineering, Southeast University, Nanjing 210096, China*
[3] *Ministry-of-Education Key Laboratory for the Synthesis and Application of Organic Functional Molecules, Hubei Collaborative Innovation Center for Advanced Organic Chemical Materials, College of Chemistry and Chemical Engineering, Hubei University, Wuhan 430062, China*
[4] *Department of Chemistry, University of North Texas, Denton, TX 76201, USA*

Received: 15 April 2020 / **Revised:** 28 July 2020 / **Accepted:** 1 August 2020

ABSTRACT

The nanoplatforms based on upconversion nanoparticles (UCNPs) have shown great promise in amplified photodynamic therapy (PDT) triggered by near-infrared (NIR) light. However, their practical *in vivo* applications are hindered by the overheating effect of 980 nm excitation and low utilization of upconversion luminescence (UCL) by photosensitizers. To solve these defects, core–satellite metal–organic framework@UCNP superstructures, composed of a single metal–organic framework (MOF) NP as the core and Nd^{3+}-sensitized UCNPs as the satellites, are designed and synthesized via a facile electrostatic self-assembly strategy. The superstructures realize a high co-loading capacity of chlorin e6 (Ce6) and rose bengal (RB) benefitted from the highly porous nature of MOF NPs, showing a strong spectral overlap between maximum absorption of photosensitizers and emission of UCNPs. The *in vitro* and *in vivo* experiments demonstrate that the dual-photosensitizer superstructures have trimodal (magnetic resonance (MR)/UCL/fluorescence (FL)) imaging functions and excellent antitumor effectiveness of PDT at 808 nm NIR light excitation, avoiding the laser irradiation-induced overheating issue. This study provides new insights for the development of highly efficient PDT nanodrugs toward precision theranostics.

KEYWORDS

core–satellite structures, upconversion nanoparticles (UCNPs), nanoscale metal–organic frameworks, photodynamic therapy, theranostics

1 Introduction

Photodynamic therapy (PDT) is a promising cancer treatment modality with low occurrence of side effects, minimal invasion, and high selectivity [1, 2]. It has been developed as an alternative approach to chemotherapy in the treatment of certain types of cancer [3, 4]. However, traditional PDT utilizing conventional photosensitizers is limited by the shallow tissue penetration of excitation light in ultraviolet to visible (UV–vis) range, confining the treatment to shallow-seated tumors [5, 6]. In order to realize deep-tissue PDT, upconversion nanoparticles (UCNPs) have been intensively explored to excite the photosensitizers due to their ability to convert low-energy near-infrared (NIR) light into high-energy UV–vis light, taking advantage of the high tissue penetration ability of NIR light [7–9]. Among the available different types of UCNPs, the Yb^{3+}-sensitized UCNPs with 980 nm excitation is the most widely used to produce upconversion luminescence (UCL) [10, 11]. However, such irradiation can cause severe overheating issues of biotissues, greatly restricting its applications in biomedicine [12–16]. In recent years, the Nd^{3+}-sensitized UCNPs with 808 nm excitation have been reported [17–19]. Due to the lowest water absorption in NIR region around 700–900 nm, the use of Nd^{3+}-sensitized UCNPs has a larger penetration depth but less heating effect, showing great promise to achieve highly efficient phototherapy *in vivo* [20–22]. The efficiency of energy transfer from UCNPs to photosensitizers is another important factor affecting therapeutic effects of UCNP-based PDT systems [23]. It is necessary to load adequate photosensitizers whose maximum absorption could significantly overlap with the narrow UCL spectra and thus utilize upconverted emission energy efficiently. Nevertheless, previously reported silica-coated UCNPs had a low loading capacity of photosensitizers or could only utilize partial UCL spectra, dramatically hindering the reactive oxygen species (ROS) production and *in vivo* PDT effects [23–26].

Nanoscale metal–organic frameworks (nMOFs), constructed from metal ions/clusters coordinated by bridging organic ligands [27], have recently emerged as an intriguing class of functional nanomaterials for biomedical applications [28–31]. nMOFs

Address correspondence to Jian Tian, jian.tian@whu.edu.cn; Shengqian Ma, Shengqian.Ma@unt.edu

have great synthetic tunability, remarkably high drug loading capacity, and good biocompatibility and biodegradability [32, 33]. These features make nMOFs ideal nanoplatforms for drug delivery [34, 35]. In this regard, photosensitizer-incorporated nMOFs (porphyrinic nMOFs for example) have been reported as a promising class of future PDT agents [36–40]. Some recent efforts have been made to combine porphyrinic nMOFs and UCNPs for enhanced PDT, and achieved relatively good therapeutic effects. For example, Cha et al. assembled porphyrinic Zr-MOF PCN-224 NPs and UCNPs into core–satellite structures under DNA mediation, showing effective tumor cells killing *in vitro* [41]. Li et al. showed that heterodimer architectures composed of porphyrinic MOFs and UCNPs realized efficient cancer treatments by combining chemotherapy and NIR-induced PDT [42]. In these studies, however, the complex synthesis of NP superstructures, the need for 980 nm laser irradiation and the relatively low utilization of UCL by porphyrinic nMOFs limited their practical PDT applications *in vivo* [41–44].

To solve the above limitations, herein we report the construction of core–satellite MOF@UCNP superstructures that can serve as a new nanotheranostic platform for effective multimodal imaging-guided PDT cancer therapy. As illustrated in Scheme 1, we loaded dual photosensitizers chlorin e6 (Ce6) and rose bengal (RB) inside highly porous MOF (UiO-68-NH_2) NPs, and further combined with the Nd^{3+}-sensitized UCNPs through electrostatic interaction to form the MOF@UCNP core–satellite superstructure (denoted as CR@MU) [45, 46]. Furthermore, this core–satellite nanostructure was modified with poly(ethylene glycol) (PEG) chains (denoted as CR@MUP) to improve its biocompatibility and biostability. CR@MUP as a PDT nanodrug may have several advantages: (1) the use of Nd^{3+}-sensitized UCNPs excited with 808 nm laser avoid the overheating issue; (2) the highly porous nature of UiO-68-NH_2 ensures sufficient co-loading of Ce6 and RB that could achieve higher energy transfer efficiency from UCNPs to photosensitizers; (3) the modification on the surface of MOF NPs can bind multiple UCNPs without affecting photosensitizers loading; (4) the UCNP and Ce6 can be used for magnetic resonance (MR)/UCL and fluorescence (FL) imaging, respectively; (5) the preparation of core–satellite nanostructures via electrostatic self-assembly is facile and highly controllable. All of these merits are further manifested by the highly effective trimodal imaging-guided photodynamic anticancer effects of CR@MUP *in vitro* and *in vivo*, implying that CR@MUP is a promising theranostic photodynamic system.

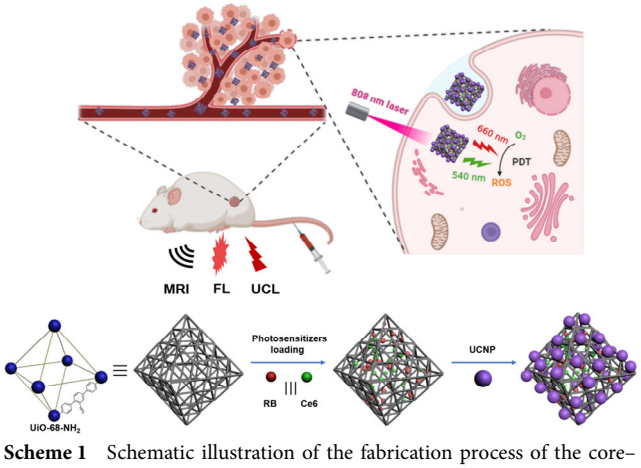

Scheme 1 Schematic illustration of the fabrication process of the core–satellite CR@MUP theranostic nanoplatform and its operation for imaging-guided photodynamic therapy.

2 Experimental

2.1 Materials

All standard synthesis reagents were purchased from commercial suppliers and used without any further purification. $RECl_3·6H_2O$ (RE = Gd, Yb, Er), RE_2O_3 (RE = Gd, Yb, Nd), oleic acid (OA, 90%), 1-octadecene (ODE, 95%), zirconyl chloride octahydrate ($ZrOCl_2·8H_2O$), 2,5-dibromobenzenamine, 4-methoxycarbonylphenylboronic acid, and trifluoroacetic acid (CF_3COOH) were obtained from Energy Chemical. Sodium hydroxide (NaOH), ammonium fluoride (NH_4F), acetic acid (CH_3COOH), 1,3-diphenylisobenzofuran (DPBF), and N,N-dimethylformamide (DMF) were purchased from Sinopharm chemical reagent. Ce6 was obtained from J&G. RB, 3-(4,5-dimethylthiazol-2-yl)-2,5-diphenyltetrazolium bromide (MTT), 2',7'-dichlorodihydrofluorescein diacetate (DCFH-DA), and Dulbecco's modified Eagle's medium (DMEM) were purchased from Wuhan Kerui Biotechnology Co., Ltd., and SH-PEG-OMe was obtained from Peng Sheng Biological.

2.2 Preparation of 808 nm-excited $NaGdF_4$:Yb,Er@$NaGdF_4$:Nd,Yb UCNP

Generally, $RECl_3·6H_2O$ (1.25 mmol, Gd:Yb:Er = 78:20:2) was added in the mixture of OA (10 mL) and ODE (15 mL). The solution was degassed by the use of nitrogen, and heated to 160 °C by vigorous stirring to form a homogeneous solution. After the solution was cooled down to room temperature, 10 mL methanol solution containing NaOH (0.2 g) and NH_4F (0.285 g) was added and stirred for 30 min. Then the system was heated to 80 °C to evaporate the methanol. After that, the system was heated to 310 °C and stirred for 1 h. When the system was cooled down to room temperature, ethanol (15 mL) was added to precipitate the NPs. Pure $NaGdF_4$:Yb,Er was dispersed in cyclohexane after centrifuged and washed with ethanol/cyclohexane (5/1). As for the core–shell $NaGdF_4$:Yb,Er@$NaGdF_4$:Nd,Yb UCNPs, the synthesis method was similar. $RE(CF_3COO)_3$ (0.5 mmol, Gd:Yb:Nd = 5:1:4) was dissolved in the mixture of OA (2.5 mL) and ODE (5 mL) at 125 °C to form the shell precursor solution. As-prepared core NPs (5 mL) were mixed with OA (5 mL) and ODE (8 mL), the mixture was heated to 70 °C under vacuum condition to remove the cyclohexane. After that, the mixture was heated to 300 °C, and the shell precursor solution was added. The system was cooled down to room temperature after stirred for 1 h. The pure $NaGdF_4$:Yb,Er@$NaGdF_4$:Nd,Yb UCNPs were obtained after washed with EtOH/cyclohexane (5/1).

2.3 Preparation of ligand-free UCNPs

Low frequency ultrasonic (LFU) NPs were obtained by removing OA with hydrochloric acid [46, 47]. Generally, the as-synthesized UCNPs (13 mg) were dispersed in 1 mL ethanol, and then 1 mL hydrochloric acid (1 M) was added. The mixture was centrifuged to get NPs (13,000 rpm, 20 min) after ultrasonic treatment, and the acid washing process was repeated one more time. The LFU NPs were washed with ethanol 3 times and redispersed in DMF for further use.

2.4 Preparation of UiO-68-NH_2

Aminotriphenyl dicarboxylic acid (amino-TPDC) was synthesized according to the reported procedure [48]. The UiO-68-NH_2 NPs were prepared using a solvothermal method. In brief, amino-TPDC (10.5 mg) and $ZrOCl_2·8H_2O$ (8.3 mg) were dissolved in DMF (1.5 mL), and then acetic acid (40 μL) was

added. The mixture was sonicated for 5 min and heated at 90 °C for 6 h. The UiO-68-NH_2 was obtained by centrifuging and washing with DMF 3 times.

2.5 Preparation of CR@UiO-68-NH_2

For Ce6 loading, the UiO-68-NH_2 solution (1 mg·mL^{-1}, 1 mL) was added with Ce6 (1 mg), and the mixture was stirred in dark. After 24 h, the NPs were washed with DMF and H_2O, and then RB aqueous solution (1 mg·mL^{-1}, 1 mL) was added and stirred in dark for 24 h. Excess RB was removed by washing with H_2O and DMF. The obtained CR@UiO-68-NH_2 solution was dispersed in DMF for further use.

2.6 Preparation of CR@MUP core–satellite NP superstructures

CR@UiO-68-NH_2 (200 μg) and LFU NPs (400 μg) were mixed in DMF (5 mL). The resulting mixture was treated with an ultrasonic processor (50 W, 20 min) and then stirred in dark for 12 h. After centrifugation (11,000 rpm, 20 min) and washed with DMF, the CR@MU NPs were obtained via the centrifugal separation of excessive LFU. To prepare CR@MUP, SH-PEG-OMe (500 μg) was added to the DMF solution of CR@MU. Then the mixture was stirred in dark for 24 h. Unbound PEG chains were removed by washing with H_2O.

2.7 Characterization

Transmission electron microscope (TEM) images were obtained from HITACHI H-7000FA TEM. Zeta potential and hydrodynamic size were measured by Malvern Zetasizer Nanoseries 90. Powder X-ray diffraction (PXRD) patterns were acquired from MiniFlex600 Focus diffractometer (Rigaku) under Cu *K*α radiation (parameters: 600 W). Fourier transform infrared (FTIR) spectra were performed using Thermo Nicolet NEXUS 470 spectrometer. UV-vis-NIR absorbance spectra were collected on Shimadzu UV-2600 spectrophotometer. UCL spectra and UCL lifetime were recorded from Edinburgh FLS980 Spectrometer with an 808 nm excitation laser. Inductively coupled plasma mass spectrometry (ICP-MS) was measured by an Analytik Jena inductively coupled plasma mass spectrometer. Laser confocal fluorescence microscope (CLSM) images were collected by Carl Zeiss NOL-LSM 710. FL imaging *in vivo* was performed using Bruker small animal live imager. Magnetic resonance imaging (MRI) *in vivo* was evaluated using Bruker BioSpec 4.7 T MRI scanning.

2.8 ROS detection *in vitro*

ROS production was monitored using DPBF as the probe. DPBF solution (8 μL, 2.7 mg·mL^{-1} in ethanol) was mixed with the sample solution (1 mL). After irradiation with 808 nm laser (1 W·cm^{-2}) for different times (0, 5, 10, 15, 20, 25, and 30 min), the UV-vis-NIR absorbance spectra were measured. The ROS productive was determined as $(I_0 - I)/I_0$ (I_0 refers to the absorbance intensity of 0 min).

2.9 Cell culture

4T1 cells were purchased from the China Center for Type Culture Collection. 4T1 cells were cultured in DMEM medium containing 10% fetal bovine serum (FBS) and 1% penicillin/streptomycin. Cells were incubated in an atmosphere at 37 °C with 5% CO_2.

2.10 FL/UCL imaging *in vitro* and cellular uptake

4T1 cells were seeded in confocal dishes for 24 h. Then the medium was replaced with DMEM medium (1 mL) containing CR@MUP and the cells were incubated with the NPs for different times (2, 4, and 8 h). After washing off the untaken CR@MUP, the cells were imaged with CLSM. For the cellular FL imaging of Ce6, the excitation wavelength was 633 nm; for the cellular FL imaging of RB, the excitation wavelength was 561 nm; and for *in vitro* UCL imaging, the excitation wavelength was 808 nm.

2.11 ROS detection in 4T1 cells

4T1 cells were cultured in 12-well plates for 24 h. After that, the medium was replaced with DMEM medium (1 mL) containing different samples and co-incubated with cells for 8 h. Then DCFH-DA was added and the irradiation was conducted (808 nm, 1 W·cm^{-2}, 5 min) after 30 min incubation. The images were obtained using an inverted fluorescence microscope.

2.12 Hemolysis assay

Mouse whole blood was centrifuged and washed with saline for five times (3,000 rpm, 5 min). The obtained pure erythrocytes were mixed with CR@MUP at different concentrations (0, 31.25, 62.5, 125, and 250 μg·mL^{-1} in saline) and incubated at 37 °C for 6 h. 100% hemolysis was achieved by mixing the erythrocytes with H_2O. After centrifugation, the UV absorption of the supernatants at 540 nm was determined.

2.13 Cytotoxicity study *in vitro*

The 4T1 cells cytotoxicity of CR@MUP was investigated using MTT assay. 4T1 cells were seeded in 96-well plates. After 24 h, various concentrations of CR@MUP (0, 12.5, 25, 50, 100, and 200 μg·mL^{-1}) were added and incubated with cells for 24 h. The medium was substituted with MTT solution (0.5 mg·mL^{-1}). After 4 h, the medium was removed and dimethyl sulphoxide (DMSO) (160 μL) was added. The UV absorption at 490 nm was measured.

2.14 Hematoxylin and eosin (H&E) staining and serum biochemical indicators

Healthy Balb/C mice were divided into two groups (n = 3) and intravenously injected with saline or CR@MUP (50 mg·kg^{-1}). The mice were sacrificed after 14 days, and the major organs (heart, liver, spleen, lung, and kidney) and serum were collected for H&E staining and biochemical indicator detection (alanine aminotransferase (ALT), aspartate aminotransferase (AST), T-bill, creatinine (CR), and uric acid (UA)).

2.15 PDT *in vitro*

4T1 cells were cultured in 96-well plates for 24 h. Then various concentrations of CR@MUP (0, 12.5, 25, 50, 100, and 200 μg·mL^{-1}) or different samples were incubated with cells for 8 h. The cells were irradiated with 808 nm laser (1 W·cm^{-2}, 5 min) after washed with phosphate buffer saline (PBS) 3 times. Following that, the MTT assay was performed to determine cell viability.

2.16 Live/dead cell viability assay

4T1 cells were seeded in 12-well plates and cultured for 24 h. After that, the medium was replaced with DMEM medium (1 mL) containing different samples and co-incubated with cells for 8 h. For light group, cells were irradiated with 808 nm laser (1 W·cm^{-2}, 5 min) after washed with PBS 3 times. An additional 24-h incubation was taken before adding calcium AM and PI. The images were taken using an inverted fluorescence microscope.

2.17 Animal model

Female Balb/C mice (16–18 g) were obtained from Beijing Vital

River Laboratory Animal Technology Co. Ltd. All the animal studies were performed in compliance with the Chinese Regulations for the Administration of Affairs Concerning Experimental Animals and approved by the Institutional Animal Care and Use Committee of Wuhan University. 5×10^6 4T1 cells were subcutaneously injected in the right-back of mice. The mice were used when the tumor volumes reached ~ 100 mm^3. Tumor volume = (tumor length) × (tumor width)^2/2.

2.18 FL/MR imaging *in vivo*

The tumor-bearing mice were intravenously injected with CR@MUP solution (25 mg·kg^{-1}), and the fluorescent images of mice at different times (0, 3, 6, 9, 12, and 24 h) were recorded by the use of a small animal live imager. The wavelength of excitation light was 650 nm, and the emitted light was filtered through a 700 nm filter. After 24 h, the mice were sacrificed, and tumors and major organs were collected to observe the biodistribution of the NPs. The *in vivo* MRI was performed on a 4.7 T MRI instrument at room temperature. Briefly, the tumor-bearing mice were injected with CR@MUP solution via the tail vein, and MR images were collected at different times (0, 3, and 6 h) after injection.

2.19 *In vivo* PDT

4T1-bearing mice were randomly divided into 6 groups (n = 3): Control, Laser, CR@MUP, C@MUP + Laser, R@MUP + Laser, and CR@MUP + Laser. Each group was intravenously injected with corresponding materials (40 mg·kg^{-1}). After 6 h, the mice in the Laser only or PDT treatment groups were irradiated with 808 nm laser (1.25 W·cm^{-2}, 5 min). The tumor volume and body weight of mice were measured every other day.

3 Results and discussion

3.1 Preparation and characterization of CR@MUP

To construct the CR@MUP, $NaGdF_4$:Yb,Er@$NaGdF_4$:Nd,Yb was firstly synthesized according to the literature with minor modifications [49], and then ligand-free UCNPs (LFU NPs, Fig. 1(a)) were obtained by washing off the OA with hydrochloric acid. After removing OA, the crystalline structure and the morphology of LFU NPs were constant, except the size was slightly decreased (Fig. S1 in the Electronic Supplementary Material (ESM)). The formation of LFU NPs was confirmed by FTIR spectroscopy, showing that the absorption peaks of OA's –CH_2 (2,914 cm^{-1}, 2,880 cm^{-1}) spectroscopy apparently disappeared (Fig. S2 in the ESM). UiO-68-NH_2 NPs were obtained with a uniform trigonal bipyramidal shape using a solvothermal method (Fig. 1(b)). After loading with dual photosensitizers Ce6 and RB, the zeta potential of UiO-68-NH_2 NPs changed from +33.1 to –14.3 mV. Such drug- loaded NPs were modified with positively charged LFU NPs via electrostatic interactions to afford the core–satellite CR@MU nanostructure. It was noted that the excessive and unbounded LFU NPs could be facially separated via centrifuge, rendering the electrostatic self-assembly process highly controllable. To obtain CR@MUP, SH-PEG-OMe was further conjugated to the surface of CR@MU nanocomposites via the strong thiol–metal interactions with LFU. In Fig. 1(c), the typical TEM images showed that the core–satellite CR@MUP superstructure was uniform and the LFU NPs were evenly distributed on the surface of single UiO-68-NH_2 NPs. The energy dispersive X-ray spectroscopy (EDS) spectrum of CR@MUP revealed the coexistence of Zr and Gd in the superstructure (Fig. S3 in the ESM). The successful fabrication of CR@MUP was further characterized by PXRD, ICP-MS, FTIR, and zeta potential measurements. The PXRD pattern (Fig. 1(d)) further confirmed that the CR@MUP nanocomposites simultaneously contained the characteristic peaks of the core UiO-68-NH_2 NPs and the satellite LFU NPs. The ICP-MS measurement revealed that the molar ratio of Zr and Gd in the CR@MUP to be 1:1.19, corresponding to about 34 LFU NPs bound to 1 UiO-68-NH_2 NP by average. The successful modification of the PEG chain was confirmed by measuring the hydrodynamic diameters and FTIR. After the surface decoration, the hydrodynamic diameter changed from 196.3 ± 4.3 to 216.0 ± 7.3 nm (Fig. 1(e)), and the absorption peaks of C–O–C (1,030–1,120 cm^{-1}) group were more obvious (Fig. S4 in the ESM). In addition, the electrostatic self-assembly process of CR@MUP was monitored stepwise by zeta potential measurements (Fig. 1(f)), and the negative zeta potential of CR@MUP was suitable for *in vivo* circulation.

Prior to further studies, the colloidal stability of CR@MUP

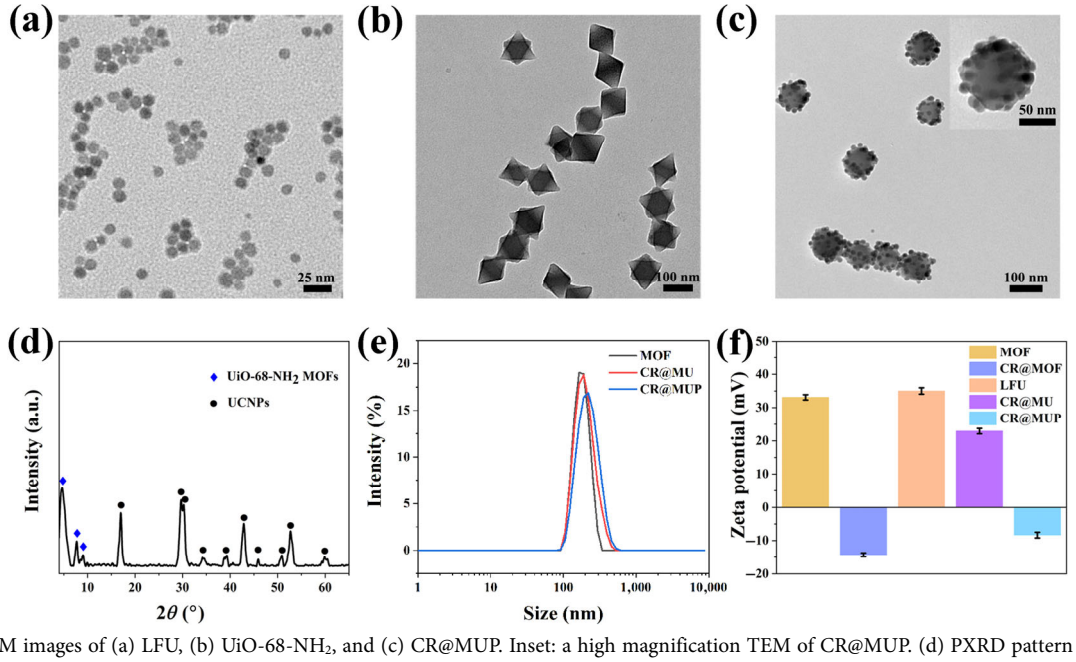

Figure 1 TEM images of (a) LFU, (b) UiO-68-NH_2, and (c) CR@MUP. Inset: a high magnification TEM of CR@MUP. (d) PXRD pattern of CR@MUP. (e) Hydrodynamic diameters of UiO-68-NH_2, CR@MU, and CR@MUP. (f) Zeta potentials of UiO-68-NH_2, CR@MOF, LFU, CR@MU, and CR@MUP.

was evaluated. The CR@MUP was suspended in saline or DMEM containing 10% FBS for 24 h and its morphology and crystallinity remained the same (Figs. S5 and S6 in the ESM). Besides, no significant decrease of photosensitizer loading was detected after 24-h incubation (Fig. S7 in the ESM). All these results collectively confirmed that CR@MUP was stable in physiological conditions and held great potential for *in vivo* applications.

3.2 *In vitro* ROS generation and FL/UCL imaging

The loading contents (LC) of Ce6 and RB in CR@MUP were obtained by UV–vis–NIR spectroscopy and calculated to be 10.5% and 10.2%, respectively, from the corresponding standard calibration curve (Fig. S8 in the ESM). Notably, these values are significantly higher than LC of photosensitizers in silica-coated UCNP systems [23–26]. The loading efficiency (LE) of Ce6 and RB in CR@MUP was calculated to be 11.7% and 11.4%, respectively. As given in Fig. 2(a), the emission of LFU NPs mainly located at about 540 and 660 nm, which coincidently overlapped with the maximum absorption of RB and Ce6, and thus ensured the efficient utilization of UCL by photosensitizers. Compared with LFU NPs, the UCL intensity at 540 and 660 nm significantly reduced after the encapsulation of RB and Ce6 into CR@MUP (Fig. 2(b)), indicating the efficient fluorescence resonance energy transfer (FRET) from LFU NPs to photosensitizers. In contrast, the porphyrinic nMOFs as photosensitizers were reported to have very weak absorption Q-bands centered at ~ 550 and ~ 645 nm, implying relatively low efficiency of UCL utilization [42]. Moreover, the UCL decay curves of LFU + MOF (physical mixture of LFU and MOF) and CR@MUP were measured to compare green and red emission lifetimes. As shown in Figs. 2(c) and 2(d), the UCL lifetime monitored at 541 nm decreased from 122 to 83 μs, and the UCL lifetime monitored at 657 nm decreased from 236 to 153 μs. The significantly shortened UCL lifetimes of CR@MUP at 541 and 657 nm further verified the efficient FRET between LFU and dual photosensitizers, which is advantageous over the UCNP-based single photosensitizer PDT system. The ROS productivity of CR@MUP was measured using DPBF. Compared with the physical mixture (CR@MOF + LFU) and the group without LFU NPs (CR@MOF), the CR@MUP group showed a more obvious decline of DPBF absorption (Fig. S9 in the ESM), suggesting the decoration of UCNPs on the surface of MOFs could increase the efficiency of energy transfer. For the group loaded with only Ce6 (C@MUP) or RB (R@MUP), a certain amount of ROS could also be produced but was significantly less than that of the CR@MUP group (Fig. 2(e)). Moreover, DCFH-DA was used as a fluorescent indicator to measure the ROS productivity in 4T1 cells for different treatment groups. The green fluorescence of cells treated with CR@MUP and 808 nm laser irradiation was more intense than the groups treated with C@MUP or R@MUP (Fig. 2(f)), indicating that more intracellular ROS was produced, consistent with the results of DPBF assay.

The cellular uptake of CR@MUP by 4T1 cells was further evaluated with the use of UCL and FL imaging. Figure 3

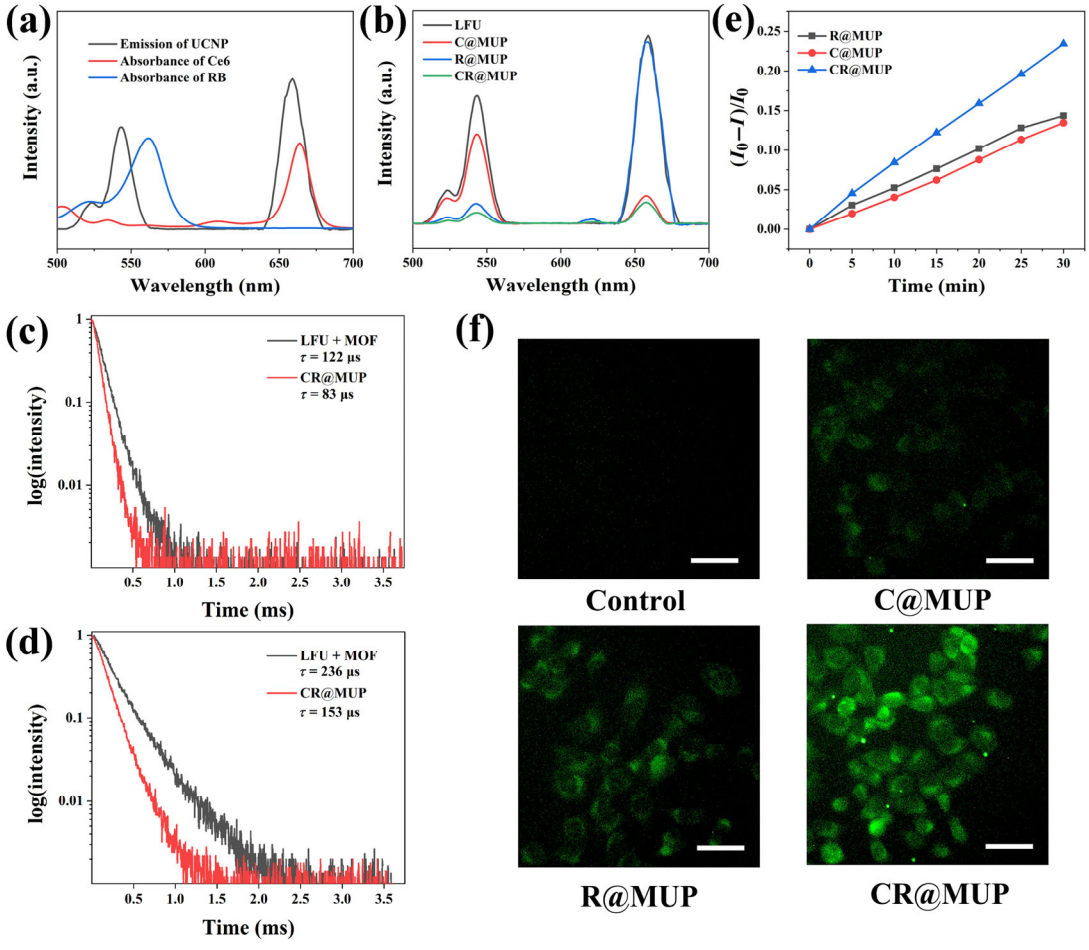

Figure 2 (a) UCL spectra of LFU and the absorption spectra of RB and Ce6. (b) UCL spectra of LFU, CR@MUP, C@MUP, and R@MUP. UCL decay curves of the emission of LFU + MOF and CR@MUP monitored at (c) 541 nm and (d) 657 nm under the 808 nm excitation wavelength. (e) ROS generation of CR@MUP, C@MUP, and R@MUP under 808 nm laser irradiation for different times. (f) Detection of intracellular ROS generation with DCFH-DA. Scale bar: 50 μm.

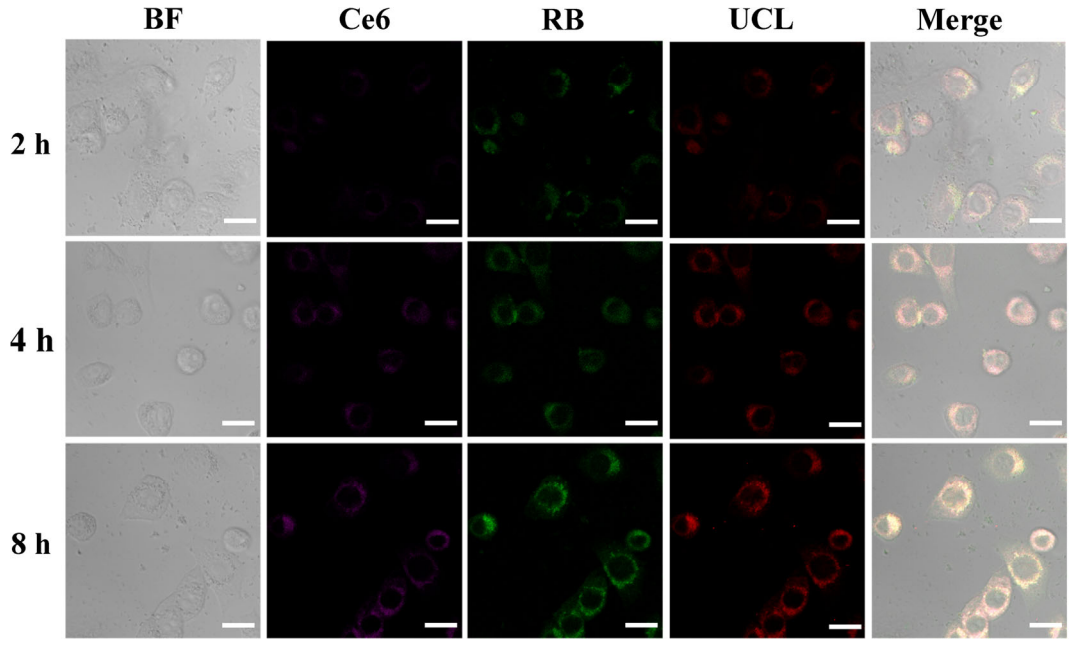

Figure 3 Confocal images of 4T1 cells incubated with CR@MUP for different time. Scale bar: 20 μm. The excitation wavelengths for the cellular FL imaging of Ce6 and RB are 633 and 561 nm, respectively. For the cellular UCL imaging, the excitation wavelength is 808 nm.

represented the upconversion luminescent microscopy (UCLM) images and fluorescence images of 4T1 cells incubated with CR@MUP for 2, 4, and 8 h at 37 °C. It was obvious that the CR@MUP NPs in the cells could radiate red luminescence upon 808 nm laser irradiation, and the intensity of red emission gradually increased with the prolonged incubation time. Moreover, Ce6, RB, and upconversion fluorescence showed intracellular co-localization, implying that the NPs were engulfed into the cells by endocytosis instead of passive adsorption. These results indicated that CR@MUP was an effective contrast agent for UCL and FL imaging and could be effectively ingested by 4T1 cells.

3.3 Biocompatibility and *in vitro* PDT effect

Before the *in vivo* utilization of CR@MUP, its biocompatibility was investigated. Red blood cells (RBCs) were incubated with different concentrations of CR@MUP (37 °C, 6 h), and no obvious hemolysis was observed (less than 2%) as shown in Fig. 4(a). Furthermore, H&E staining and serum biochemical index of mice treated with CR@MUP (14 d) were carried out, and the results showed no obvious damage to major organs (Figs. S11 and S12 in the ESM). Overall, CR@MUP possessed good biocompatibility without significant side effects at the dose tested. Moreover, the heating effect of laser was evaluated using Balb/c mice. The temperature of the irradiated region after 5 min exposure to 808 nm laser was below 42 °C, causing no damage to mice. Under the same condition, however, 980 nm laser could heat the irradiated region to above 50 °C and severely burn the skin (Fig. S13 in the ESM). These findings suggested that 808 nm excitation had a much weaker tissue heating effect and was more suitable for biological applications.

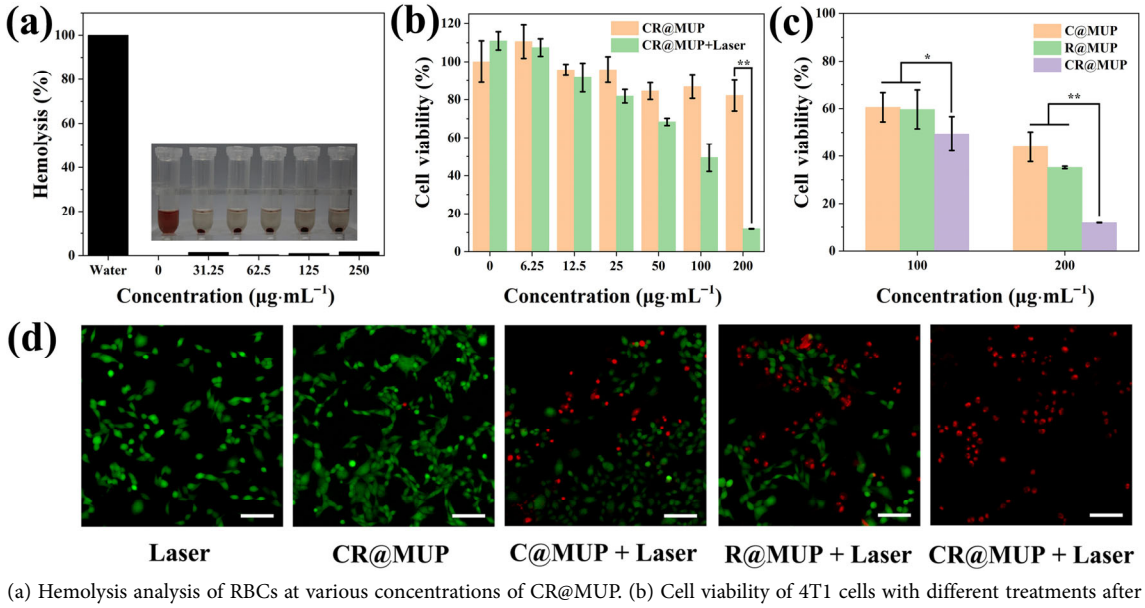

Figure 4 (a) Hemolysis analysis of RBCs at various concentrations of CR@MUP. (b) Cell viability of 4T1 cells with different treatments after incubated with various concentrations of CR@MUP. (c) Cell viability of 4T1 cells irradiated with 808 nm laser after incubated with different NP. (d) Live/dead assay of 4T1 cells after different treatments. Scale bar: 100 μm. *$p < 0.05$ and **$p < 0.01$.

MTT assay was then applied to evaluate the PDT effect of CR@MUP in 4T1 cells. CR@MUP showed no obvious toxicity to 4T1 cells even at a concentration of 200 μg·mL^{-1}. Once irradiated with 808 nm laser, the cell viability significantly decreased as the CR@MUP concentration increased (Fig. 4(b)), and its cell death rate was higher than the single-photosensitizer nanosystems (Fig. 4(c)). Furthermore, the PDT effects of CR@MUP, C@MUP, and R@MUP were compared by using live/dead cell viability assay, in which live cells and dead cells were stained with calcein acetoxymethyl ester (calcein AM, green) and propidium iodide (PI, red), respectively. As shown in Fig. 4(d), for the cells treated with 808 nm laser or CR@MUP only, widespread green fluorescence signal appeared, indicating that these treatments didn't affect cell viability. Comparatively, obvious red fluorescence signal and little green signal were observed after the laser irradiation in the group treated with CR@MUP, which indicated strong PDT-induced cytotoxicity. In contrast, under the same laser condition, the more green fluorescence signal was detected in the groups treated by single-photosensitizer nanosystems, suggesting the higher PDT potency of the dual-photosensitizer nanosystem.

3.4 *In vivo* stability and tumor imaging

The *in vivo* stability of the CR@MUP superstructure was evaluated by measuring the Zr/Gd ratio of the tumor. CR@MUP and CR@MU were injected through the tail vein, and tumor tissues were collected for ICP-MS analysis after 24 h. Compared with CR@MU, the Zr/Gd ratio of CR@MUP hardly changed before and after injection (Fig. S14(a) in the ESM), indicating the better stability *in vivo* after the PEG chain functionalization. Besides, tumor enrichment of CR@MUP (determined with Zr content) increased to 2.54% ID g^{-1} (Fig. S14(b) in the ESM), which suggested that the PEG modification could increase the accumulation of the superstructure inside tumors.

To further evaluate the tumor accumulation and imaging effect of CR@MUP *in vivo*, BALB/c mice bearing 4T1 xenograft tumors were intravenously injected with CR@MUP and the fluorescence signal was recorded at different time points. As shown in Fig. 5(a), the fluorescence signal appeared at the tumor site 3 h after injection and reached the strongest at 6 h, which provided a basis for the selection of the 808 nm laser irradiation time point for subsequent *in vivo* PDT. In addition, the main organs and tumors were isolated to study the biodistribution of CR@MUP at 24 h post-injection. Figure S15 in the ESM showed that CR@MUP was mainly concentrated in tumors due to the enhanced permeability and retention (EPR) effect. Besides, only faint fluorescence signals could be detected in liver, spleen, and lung, while scarcely any signal was observed in heart, intestine, and kidney. These results indicated that CR@MUP was cleared primarily by liver and had lung and spleen retention. The targeting and enrichment behavior of CR@MUP on tumor sections was also investigated by MRI. As shown in Fig. 5(b), brighter T_1-weighted images of the aqueous solutions of CR@MUP were observed with the increased Gd^{3+} concentration, and the longitudinal relaxivity (r_1) was calculated to be 5.74 mM^{-1}·s^{-1}, which was suitable for T_1-weighted imaging. The *in vivo* MRI was further evaluated with 4T1 tumor-bearing mice. T_1-weighted images of mice were recorded after intravenous injection of CR@MUP and the signal of the tumor region gradually became stronger in 6 h post-injection (Figs. 5(c) and 5(d)), which was consistent with the FL imaging results. The presented results suggested that CR@MUP could efficiently enrich at tumor sites due to the EPR effect, and could be an effective MR/FL contrast agent to guide *in vivo* PDT.

3.5 *In vivo* PDT effect

Encouraged by the effective PDT *in vitro* and tumor accumulation of CR@MUP *in vivo*, its antitumor effect on 4T1 tumor

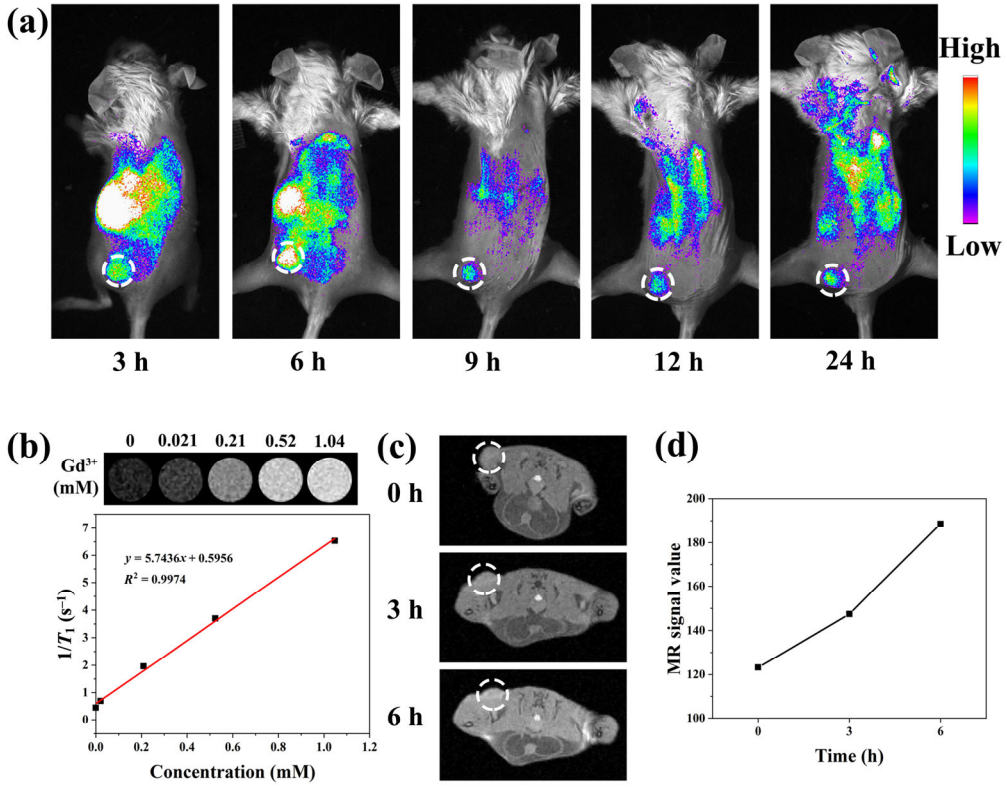

Figure 5 (a) Fluorescence images of 4T1 tumor-bearing mice at different times after intravenous injection of CR@MUP (white circles indicate the tumors). (b) T_1-weighted MR images and T_1 relaxation curves of CR@MUP. (c) T_1-weighted MR images and (d) quantification analysis of MRI signals of 4T1 tumor-bearing mice treated with CR@MUP (white circles indicate the tumors).

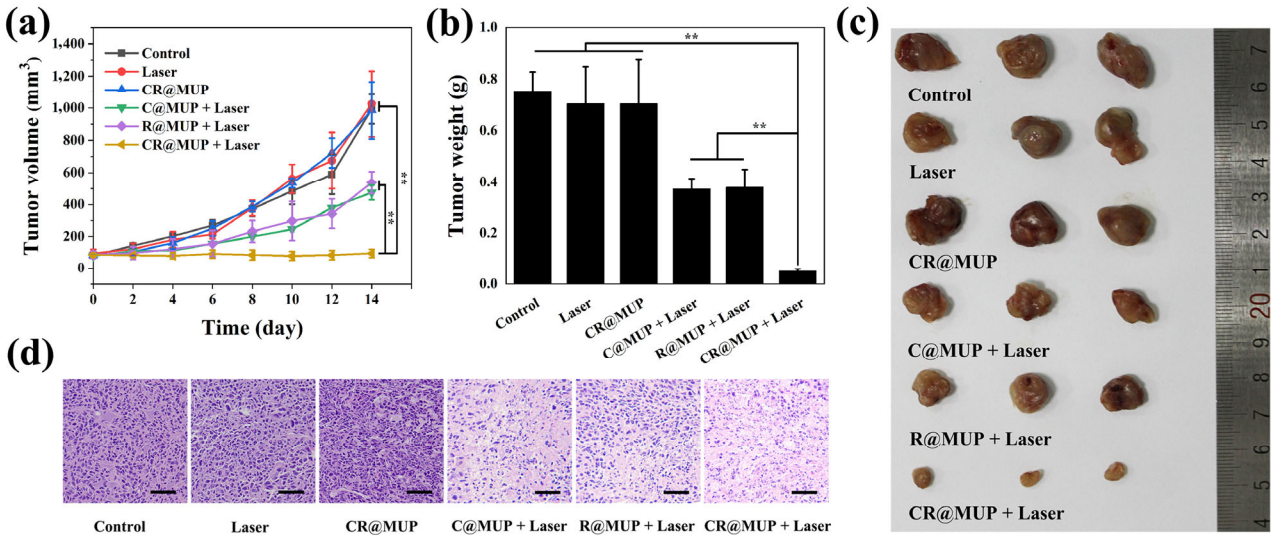

Figure 6 (a) Tumor volumes of mice in different groups after various treatments. (b) Tumor weights of mice in different treatment groups. (c) Digital photographs and (d) H&E staining of harvested 4T1 tumors after various treatments. Scale bar: 50 μm. $^{**}p < 0.01$.

xenograft mouse model was validated. The mice were divided into 6 groups when the tumor volume reached ~ 100 mm^3: Control, Laser, CR@MUP, C@MUP + Laser, R@MUP + Laser, and CR@MUP + Laser. According to the results of MR/FL bimodal imaging, the mice were irritated with 808 nm laser at 6 h post-injection. The body weight and tumor volume were recorded every 2 days. During 14 days of treatment, no significant change in body weight was observed among all groups, indicating the low toxicity of these treatments (Fig. S16 in the ESM). For the group only treated with laser or CR@MUP, the tumor volume and tumor weight were almost the same as the control group, suggesting that irradiation or CR@MUP had no inhibition on tumors. Meanwhile, for the mice treated with C@MUP and R@MUP, the tumor growth was significantly suppressed after 808 nm irradiation, which benefitted from the PDT effect of Ce6 or RB. Compared with the single-photosensitizer loaded NPs, the antitumor effect of CR@MUP + Laser group was more obvious, and the tumor growth was completely suppressed (Figs. 6(a) and 6(b)). The tumor photograph *ex vivo* also showed that the tumor size was the smallest after the treatment with CR@MUP and laser (Fig. 6(c)). To further validate the PDT effect, H&E staining was performed on tumors harvested after the treatment in each group. It was observed that the CR@MUP + Laser group had the most obvious damage to tumors (Fig. 6(d)). The *in vivo* experiments demonstrated that CR@MUP had an excellent PDT effect and could entirely inhibit tumor growth without affecting the quality of mice's life.

4 Conclusions

In summary, core–satellite MOF@UCNP superstructures were successfully fabricated via electrostatic self-assembly. The superstructures realized high co-loading content of dual photosensitizers, whose maximum absorption overlapped perfectly with the UCL spectra under 808 nm excitation, and thus took full advantage of the highly emissive upconversion to generate large quantities of cytotoxic ROS for efficient antitumor therapy. The dual-photosensitizer superstructure (CR@MUP) exhibited higher PDT efficacy than single-photosensitizer nanosystems as validated by *in vivo* and *in vitro* experiments. Moreover, the MR, UCL, and FL imaging capabilities of CR@MUP enabled trimodal imaging-guided PDT. Our work combined the advantages of UCNPs and nMOFs to realize highly effective photodynamic cancer therapy with minimized overheating effect, providing new insights into the development of theranostic photodynamic systems.

Acknowledgements

This work was financially supported by National Natural Science Foundation of China (NSFC) (Nos. 21601140 and 21871214), the Fundamental Research Funds for the Central Universities, and Open Research Fund of State Key Laboratory of Bioelectronics.

Electronic Supplementary Material: Supplementary materials (TEM images of UCNPs and LFU, FTIR spectra, supporting data for the stability, absorption spectra, H&E staining assay, blood biochemical assay, temperature changes after irradiation, ICP-MS assay, and fluorescence images of isolated organs and body weights of the mice after PDT) is available in the online version of this article at https://doi.org/10.1007/s12274-020-3025-0.

References

[1] Lovell, J. F.; Liu, T. W. B.; Chen, J.; Zheng, G. Activatable photosensitizers for imaging and therapy. *Chem. Rev.* **2010**, *110*, 2839–2857.

[2] Ye, S. Y.; Rao, J. M.; Qiu, S. H.; Zhao, J. L.; He, H.; Yan, Z. L.; Yang, T.; Deng, Y. B.; Ke, H. T.; Yang, H. et al. Rational design of conjugated photosensitizers with controllable photoconversion for dually cooperative phototherapy. *Adv. Mater.* **2018**, *30*, 1801216.

[3] Lucky, S. S.; Soo, K. C.; Zhang, Y. Nanoparticles in photodynamic therapy. *Chem. Rev.* **2015**, *115*, 1990–2042.

[4] Chen, W. S.; Ouyang, J.; Liu, H.; Chen, M.; Zeng, K.; Sheng, J. P.; Liu, Z. J.; Han, Y. J.; Wang, L. Q.; Li, J. et al. Black phosphorus nanosheet-based drug delivery system for synergistic photodynamic/photothermal/chemotherapy of cancer. *Adv. Mater.* **2017**, *29*, 1603864.

[5] Fan, W. P.; Huang, P.; Chen, X. Y. Overcoming the Achilles' heel of photodynamic therapy. *Chem. Soc. Rev.* **2016**, *45*, 6488–6519.

[6] Deng, K. R.; Li, C. X.; Huang, S. S.; Xing, B. G.; Jin, D. Y.; Zeng, Q. G.; Hou, Z. Y.; Lin, J. Recent progress in near infrared light triggered photodynamic therapy. *Small* **2017**, *13*, 1702299.

[7] Wang, C.; Cheng, L.; Liu, Z. Upconversion nanoparticles for photodynamic therapy and other cancer therapeutics. *Theranostics* **2013**, *3*, 317–330.

[8] Li, F. Y.; Du, Y.; Liu, J. N.; Sun, H.; Wang, J.; Li, R. Q.; Kim, D.; Hyeon, T.; Ling, D. S. Responsive assembly of upconversion nanoparticles for pH-activated and near-infrared-triggered photodynamic therapy of deep tumors. *Adv. Mater.* **2018**, *30*, 1802808.

[9] Liu, Y. Y.; Zhang, J. W.; Zuo, C. J.; Zhang, Z.; Ni, D. L.; Zhang, C.; Wang, J.; Zhang, H.; Yao, Z. W.; Bu, W. B. Upconversion nanophotosensitizer targeting into mitochondria for cancer apoptosis induction and cyt c fluorescence monitoring. *Nano Res.* **2016**, *9*, 3257–3266.

[10] Fan, W. P.; Bu, W. B.; Shi, J. L. On the latest three-stage development of nanomedicines based on upconversion nanoparticles. *Adv. Mater.* **2016**, *28*, 3987–4011.

[11] Yan, S. Q.; Zeng, X. M.; Tang, Y. A.; Liu, B. F.; Wang, Y.; Liu, X. G. Activating antitumor immunity and antimetastatic effect through polydopamine-encapsulated core–shell upconversion nanoparticles. *Adv. Mater.* **2019**, *31*, 1905825.

[12] Zhou, B.; Shi, B. Y.; Jin, D. Y.; Liu, X. G. Controlling upconversion nanocrystals for emerging applications. *Nat. Nanotechnol.* **2015**, *10*, 924–936.

[13] Bai, G. X.; Tsang, M. K.; Hao, J. H. Luminescent ions in advanced composite materials for multifunctional applications. *Adv. Funct. Mater.* **2016**, *26*, 6330–6350.

[14] Zhang, D. D.; Wen, L. W.; Huang, R.; Wang, H. H.; Hu, X. L.; Xing, D. Mitochondrial specific photodynamic therapy by rare-earth nanoparticles mediated near-infrared graphene quantum dots. *Biomaterials* **2018**, *153*, 14–26.

[15] He, S.; Johnson, N. J. J.; Huu, V. A. N.; Huang, Y. R.; Almutairi, A. Leveraging spectral matching between photosensitizers and upconversion nanoparticles for 808 nm-activated photodynamic therapy. *Chem. Mater.* **2018**, *30*, 3991–4000.

[16] Chen, Y.; Ren, J. L.; Tian, D.; Li, Y. C.; Jiang, H.; Zhu, J. T. Polymer-upconverting nanoparticle hybrid micelles for enhanced synergistic chemo-photodynamic therapy: Effects of emission-absorption spectral match. *Biomacromolecules* **2019**, *20*, 4044–4052.

[17] Wang, Y. F.; Liu, G. Y.; Sun, L. D.; Xiao, J. W.; Zhou, J. C.; Yan, C. H. Nd^{3+}-sensitized upconversion nanophosphors: Efficient *in vivo* bioimaging probes with minimized heating effect. *ACS Nano* **2013**, *7*, 7200–7206.

[18] Liu, B.; Chen, Y. Y.; Li, C. X.; He, F.; Hou, Z. Y.; Huang, S. S.; Zhu, H. M.; Chen, X. Y.; Lin, J. Poly(acrylic acid) modification of Nd^{3+}-sensitized upconversion nanophosphors for highly efficient UCL imaging and pH-responsive drug delivery. *Adv. Funct. Mater.* **2015**, *25*, 4717–4729.

[19] Hou, Z. Y.; Deng, K. R.; Wang, M. F.; Liu, Y. H.; Chang, M. Y.; Huang, S. S.; Li, C. X.; Wei, Y.; Cheng, Z. Y.; Han, G. et al. Hydrogenated titanium oxide decorated upconversion nanoparticles: Facile laser modified synthesis and 808 nm near-infrared light triggered phototherapy. *Chem. Mater.* **2019**, *31*, 774–784.

[20] Ai, X. Z.; Ho, C. J. H.; Aw, J.; Attia, A. B. E.; Mu, J.; Wang, Y.; Wang, X. Y.; Wang, Y.; Liu, X. G.; Chen, H. B. et al. *In vivo* covalent cross-linking of photon-converted rare-earth nanostructures for tumour localization and theranostics. *Nat. Commun.* **2016**, *7*, 10432.

[21] Li, Y.; Tang, J. L.; Pan, D. X.; Sun, L. D.; Chen, C. Y.; Liu, Y.; Wang, Y. F.; Shi, S.; Yan, C. H. A versatile imaging and therapeutic platform based on dual-band luminescent lanthanide nanoparticles toward tumor metastasis inhibition. *ACS Nano* **2016**, *10*, 2766–2773.

[22] Liu, B.; Li, C. X.; Yang, P. P.; Hou, Z. Y.; Lin, J. 808-nm-light-excited lanthanide-doped nanoparticles: Rational design, luminescence control and theranostic applications. *Adv. Mater.* **2017**, *29*, 1605434.

[23] Lu, S.; Tu, D. T.; Hu, P.; Xu, J.; Li, R. F.; Wang, M.; Chen, Z.; Huang, M. D.; Chen, X. Y. Multifunctional nano-bioprobes based on rattle-structured upconverting luminescent nanoparticles. *Angew. Chem., Int. Ed.* **2015**, *54*, 7915–7919.

[24] Idris, N. M.; Gnanasammandhan, M. K.; Zhang, J.; Ho, P. C.; Mahendran, R.; Zhang, Y. *In vivo* photodynamic therapy using upconversion nanoparticles as remote-controlled nanotransducers. *Nat. Med.* **2012**, *18*, 1580–1585.

[25] Liang, L. E.; Care, A.; Zhang, R.; Lu, Y. Q.; Packer, N. H.; Sunna, A.; Qian, Y.; Zvyagin, A. V. Facile assembly of functional upconversion nanoparticles for targeted cancer imaging and photodynamic therapy. *ACS Appl. Mater. Interfaces* **2016**, *8*, 11945–11953.

[26] Xu, J. T.; Yang, P. P.; Sun, M. D.; Bi, H. T.; Liu, B.; Yang, D.; Gai, S. L.; He, F.; Lin, J. Highly emissive dye-sensitized upconversion nanostructure for dual-photosensitizer photodynamic therapy and bioimaging. *ACS Nano* **2017**, *11*, 4133–4144.

[27] Wang, S. Z.; McGuirk, C. M.; d'Aquino, A.; Mason, J. A.; Mirkin, C. A. Metal–organic framework nanoparticles. *Adv. Mater.* **2018**, *30*, 1800202.

[28] Horcajada, P.; Chalati, T.; Serre, C.; Gillet, B.; Sebrie, C.; Baati, T.; Eubank, J. F.; Heurtaux, D.; Clayette, P.; Kreuz, C. et al. Porous metal–organic-framework nanoscale carriers as a potential platform for drug delivery and imaging. *Nat. Mater.* **2010**, *9*, 172–178.

[29] Zhang, L. Y.; Liu, C.; Gao, Y.; Li, Z. H.; Xing, J.; Ren, W. Z.; Zhang, L. L.; Li, A. G.; Lu, G. M.; Wu, A. G. et al. ZD2-engineered gold nanostar@metal-organic framework nanoprobes for T_1-weighted magnetic resonance imaging and photothermal therapy specifically toward triple-negative breast cancer. *Adv. Healthcare Mater.* **2018**, *7*, 1801144.

[30] He, Z. M.; Huang, X. L.; Wang, C.; Li, X. L.; Liu, Y. J.; Zhou, Z. J.; Wang, S.; Zhang, F. W.; Wang, Z. T.; Jacobson, O. et al. A catalase-like metal-organic framework nanohybrid for O_2-evolving synergistic chemoradiotherapy. *Angew. Chem., Int. Ed.* **2019**, *58*, 8752–8756.

[31] Neufeld, M. J.; DuRoss, A. N.; Landry, M. R.; Winter, H.; Goforth, A. M.; Sun, C. Co-delivery of PARP and PI3K inhibitors by nanoscale metal–organic frameworks for enhanced tumor chemoradiation. *Nano Res.* **2019**, *12*, 3003–3017.

[32] Lu, K. D.; Aung, T.; Guo, N. N.; Weichselbaum, R.; Lin, W. B. Nanoscale metal–organic frameworks for therapeutic, imaging, and sensing applications. *Adv. Mater.* **2018**, *30*, 1707634.

[33] Zhang, Z.; Sang, W.; Xie, L. S.; Dai, Y. L. Metal-organic frameworks for multimodal bioimaging and synergistic cancer chemotherapy. *Coordin. Chem. Rev.* **2019**, *399*, 213022.

[34] Sun, C. Y.; Qin, C.; Wang, C. G.; Su, Z. M.; Wang, S.; Wang, X. L.; Yang, G. S.; Shao, K. Z.; Lan, Y. Q.; Wang, E. B. Chiral nanoporous metal-organic frameworks with high porosity as materials for drug delivery. *Adv. Mater.* **2011**, *23*, 5629–5632.

[35] Cheng, H.; Zhu, J. Y.; Li, S. Y.; Zeng, J. Y.; Lei, Q.; Chen, K. W.; Zhang, C.; Zhang, X. Z. An O_2 Self-sufficient biomimetic nanoplatform for highly specific and efficient photodynamic therapy. *Adv. Funct. Mater.* **2016**, *26*, 7847–7860.

[36] Lu, K. D.; He, C. B.; Lin, W. B. Nanoscale metal–organic framework for highly effective photodynamic therapy of resistant head and neck cancer. *J. Am. Chem. Soc.* **2014**, *136*, 16712–16715.

[37] Park, J.; Jiang, Q.; Feng, D. W.; Mao, L. Q.; Zhou, H. C. Size-controlled synthesis of porphyrinic metal–organic framework and functionalization for targeted photodynamic therapy. *J. Am. Chem. Soc.* **2016**, *138*, 3518–3525.

[38] Min, H.; Wang, J.; Qi, Y. Q.; Zhang, Y. L.; Han, X. X.; Xu, Y.; Xu, J. C.; Li, Y.; Chen, L.; Cheng, K. M. et al. Biomimetic metal–organic framework nanoparticles for cooperative combination of antiangiogenesis and photodynamic therapy for enhanced efficacy. *Adv. Mater.* **2019**, *31*, 1808200.

[39] Ni, K. Y.; Luo, T. K.; Lan, G. X.; Culbert, A.; Song, Y.; Wu, T.; Jiang, X. M.; Lin, W. B. A nanoscale metal–organic framework to mediate photodynamic therapy and deliver CpG oligodeoxynucleotides to enhance antigen presentation and cancer immunotherapy. *Angew. Chem.* **2020**, *132*, 1124–1128.

[40] Zhu, W. J.; Yang, Y.; Jin, Q. T.; Chao, Y.; Tian, L. L.; Liu, J. J.; Dong, Z. L.; Liu, Z. Two-dimensional metal-organic-framework as a unique theranostic nano-platform for nuclear imaging and chemo-photodynamic cancer therapy. *Nano Res.* **2019**, *12*, 1307–1312.

[41] He, L. C.; Brasino, M.; Mao, C. C.; Cho, S.; Park, W.; Goodwin, A. P.; Cha, J. N. DNA-assembled core-satellite upconverting-metal-organic framework nanoparticle superstructures for efficient photodynamic therapy. *Small* **2017**, *13*, 1700504.

[42] Li, Y. F.; Di, Z. H.; Gao, J. H.; Cheng, P.; Di, C. Z.; Zhang, G.; Liu, B.; Shi, X. H.; Sun, L. D.; Li, L. et al. Heterodimers made of upconversion nanoparticles and metal–organic frameworks. *J. Am.*

Chem. *Soc*. **2017**, *139*, 13804–13810.

[43] Shao, Y. L.; Liu, B.; Di, Z. H.; Zhang, G.; Sun, L. D.; Li, L. L.; Yan, C. H. Engineering of upconverted metal–organic frameworks for near-infrared light-triggered combinational photodynamic/chemo-/immunotherapy against hypoxic tumors. *J*. *Am*. *Chem*. *Soc*. **2020**, *142*, 3939–3946.

[44] Liu, C.; Liu, B.; Zhao, J.; Di, Z. H.; Chen, D. Q.; Gu, Z. J.; Li, L. L.; Zhao, Y. L. Nd^{3+}-sensitized upconversion metal–organic frameworks for mitochondria-targeted amplified photodynamic therapy. *Angew*. *Chem*., *Int*. *Ed*. **2020**, *59*, 2634–2638.

[45] Lv, R. C.; Yang, D.; Yang, P. P.; Xu, J. T.; He, F.; Gai, S. L.; Li, C. X.; Dai, Y. L.; Yang, G. X.; Lin, J. Integration of upconversion nanoparticles and ultrathin black phosphorus for efficient photodynamic theranostics under 808 nm near-infrared light irradiation. *Chem*. *Mater*. **2016**, *28*, 4724–4734.

[46] Yuan, Z.; Zhang, L.; Li, S. Z.; Zhang, W. N.; Lu, M.; Pan, Y.; Xie, X. J.; Huang, L.; Huang, W. Paving metal–organic frameworks with upconversion nanoparticles via self-assembly. *J*. *Am*. *Chem*. *Soc*. **2018**, *140*, 15507–15515.

[47] Liu, J. N.; Bu, W. B.; Pan, L. M.; Zhang, S. J.; Chen, F.; Zhou, L. P.; Zhao, K. L.; Peng, W. J.; Shi, J. L. Simultaneous nuclear imaging and intranuclear drug delivery by nuclear-targeted multifunctional upconversion nanoprobes. *Biomaterials* **2012**, *33*, 7282–7290.

[48] He, C. B.; Lu, K. D.; Lin, W. B. Nanoscale metal–organic frameworks for real-time intracellular pH sensing in live cells. *J*. *Am*. *Chem*. *Soc*. **2014**, *136*, 12253–12256.

[49] Zeng, L. Y.; Pan, Y. W.; Zou, R. F.; Zhang, J. C.; Tian, Y.; Teng, Z. G.; Wang, S. J.; Ren, W. Z.; Xiao, X. S.; Zhang, J. C. et al. 808 nm-excited upconversion nanoprobes with low heating effect for targeted magnetic resonance imaging and high-efficacy photodynamic therapy in HER2-overexpressed breast cancer. *Biomaterials* **2016**, *103*, 116–127.